Patch-based Directional Redundant Wavelets in Compressed Sensing Parallel MRI with Radial Sampling Trajectory

***Jing Ye*[1], *Xiaobo Qu*[1*], *Hua Guo*[2], *Yunsong Liu*[1], *Di Guo*[3], *Zhong Chen*[1]**

[1]*Department of Electronic Science, Xiamen University, Xiamen, China.*

[2]*Center for Biomedical Imaging Research, Department of Biomedical Engineering, Tsinghua University, Beijing, China.*

[3]*School of Computer and Information Engineering, Xiamen University of Technology, Xiamen, China.*

Corresponding authors. Tel.: +86-592-2181712; fax: +86-592-2189426.

E-mail address: quxiaobo@xmu.edu.cn.

Abstract: Compressed sensing has been shown promising to speed up magnetic resonance imaging, and its combination with partially parallel imaging can further accelerate the data acquisition. For compressed sensing, a sparser representation of an image usually leads to lower reconstruction errors. Recently, a patch-based directional wavelets (PBDW), providing an adaptive sparse representation of image patches with geometric information, has been proposed in compressed sensing MRI to improve the edge reconstruction. However, it is still unknown how to incorporate PBDW into partially parallel imaging. In this work, we propose to use patch-based directional redundant wavelets (PBDRW) as an adaptive sparsifying transform in compressed sensing sensitivity encoding, and wed the new method with radial sampling to achieve higher acceleration factors. Results from simulation and *in vivo* data indicate that PBDRW in sensitivity encoding achieves lower reconstruction errors and preserves more image details than traditional total variation and wavelets.

Keywords: MRI, parallel imaging, compressed sensing, wavelets, radial sampling.

1. Introduction

Magnetic resonance imaging (MRI), as a noninvasive detection technique, has been widely used to investigate biological structures. However, MRI is limited due to time-consuming encoding in phase encoding directions and/or in temporal dimensions, etc. In order to accelerate the imaging, partially parallel imaging (PPI) [1-5] is adopted in commercial scanners with phase array receiver coils. In PPI, an array of receiver coils collects more information than that with a single coil. PPI can be roughly classified in k-space and image domains according to which domain the reconstruction method operates. In the k-space domain, typical methods are simultaneous acquisition of spatial harmonics [6, 7], generalized auto-calibrating partially parallel acquisitions [8-10], and iterative self-consistent parallel imaging reconstruction [11, 12]. In the image domain, sensitivity encoding (SENSE) [1, 13-15] is a typical method. The SENSE MRI is based on receiver sensitivity, which has an encoding effect complementary to gradient encoding [1]. Thus, imaging time can be saved when the undersampling data are received by multiple receiver coils in parallel scanning.

Compressed sensing was introduced to MRI to accelerate the imaging from the aspect of sparse signal processing [16-18]. This new technology is called CS-MRI for short. The CS-MRI tries to reconstruct the faithful magnetic resonance (MR) images from undersampled data, and consequently save the imaging time. A successful CS-MRI is based on three requirements: an sparse representation, artifact incoherence, and an effective numerical algorithm [16]. For the sparse representation, traditional representations include wavelets transform and finite difference [16]. Recently, Qu *et al.* proposed patch-based directional wavelets (PBDW) [19] in CS-MRI to provide an adaptive sparse representation, but it has not been combined with parallel imaging. PBDW outperforms the traditional 2D wavelets and finite difference in edge preserving. For artifact incoherence, it means that artifact should be incoherent with sparse representation. For MRI, the distribution of artifacts is seriously affected by the k-space sampling trajectory. For example, compared with Cartesian undersampling, a non-Cartesian undersampling trajectory can enhance the artifact incoherence [20, 21]. Furthermore, non-Cartesian sampling trajectories usually lead to rapid k-space coverage thus speed up encoding [21] and the radial sampling is a typical non-Cartesian sampling trajectory.

In this paper, we proposed to use patch-based directional redundant wavelets (PBDRW) as an adaptive sparsifying method in compressed sensing sensitivity encoding (CS-SENSE), and combine the new method with radial sampling to achieve higher acceleration factors. An alternating direction method with continuation algorithm is derived to solve this MRI reconstruction model. Results from simulation and *in vivo* data indicate that, using the radial undersampled data, the PBDRW based CS-SENSE provides lower reconstruction errors and preserves more details than the conventional sparsifying transforms based CS-SENSE.

2. Materials and methods

2.1 SENSE

On an MRI scanner with Q channel receiver coils, the information acquired in the field of view from q^{th} channel will be weighted by the coil sensitivity $\mathbf{C}_q$ (q=1, 2…Q). Let the k-space of q^{th} channel be $\mathbf{y}_q \in \mathbb{C}^{M\times 1}$, the SENSE data acquisition model [1] is

$$\mathbf{y}_q = \mathbf{F}_\mathbf{T}(\mathbf{C}_q\mathbf{x}), \tag{1}$$

where $\mathbf{F_T}(\cdot)$ is an operator that represents a transformation from image domain to k-space domain, $\mathbf{x} \in \mathbb{C}^{N\times 1}$ is an unknown image to be reconstructed in the full field of view .

2.2 NUFFT

As mentioned above, radial sampling technique has advantages in sampling speed [21-24]. Special pulse sequences are used to achieve specific sampling patterns, e.g. radial sampling [25, 26]. Consequently, the fast Fourier transform (FFT) is no longer applicable directly on the sampled k-space data. A non-uniform fast Fourier transform (NUFFT)[27] is applied in this case since it handles the sampled data located on non-Cartesian grids. Radial sampling in k-space and NUFFT has also been used in parallel MRI before [21, 23] .

2.3 CS-MRI

2.3.1 General CS-MRI

In the traditional CS-MRI methods, typical two-dimensional (2D) separable wavelet transform was commonly used [16, 28]. This typical transform fails to sparsely represent the geometric patterns along the singularities [29]. In traditional CS parallel MRI methods, total variation (TV) [30-32] are also widely used. However, TV is easy to generate staircase artifacts in reconstruction. Therefore, some new transforms are desired to sparsely represent MR images. For example, a dictionary pre-learned from a reference image can improve the quality of reconstructed images [33-35]. The PBDW [19] is a sparser representation but with low training complexity since only geometric directions need to be learnt from a pre-reconstructed image. However, all these new transforms neither are investigated in parallel imaging nor in realistic non-Cartesian sampling. Besides, there is still concern that the NUFFT or k-space re-gridding may affect the advantage of these patch-based images reconstruction[36].

2.3.2 PBDW-based CS-MRI

Compared with the traditional sparse representation, PBDW provides a sparser representation of image edges by arranging pixels according to geometric directions [19, 29, 37]. The Fig. 1 shows the flowchart of PBDW-based CS-MRI reconstruction. In PBDW, geometric directions are learnt from a reference image, which is reconstructed using a typical method, e.g. shift-invariant discrete wavelet transform (SIDWT). SIDWT is used as it can mitigate blocky artifacts generated by the general orthogonal wavelets [19]. To further improve the result, one can alternate the process of geometric direction training and image reconstruction and twice is good enough as recommended in [19]. The process of estimating directions are detailed in [19].

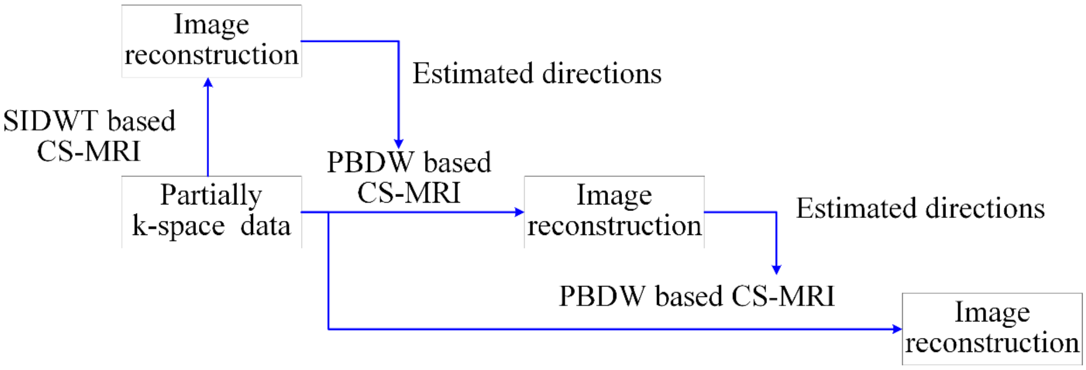

Fig. 1 Flowchart of the PBDW-based CS-MRI.

2.3.3 Redundant-wavelets-based PBDW

As the mentioned above, redundant wavelets, which is shift invariant, is always more helpful in suppress artifacts for image reconstruction [19] than orthogonal wavelets. However, the PBDW [19] proposed by Qu *et al.* is based on the 1D Haar orthogonal wavelets, and the use of redundant wavelets as an transform can preserve more features. Therefore, the redundant-wavelets-based PBDW (PBDRW) is applied in our experiments. The direction wavelets PBDRW in this paper are 1D wavelets, of which the basis are shown in Fig. 2. It clearly show how the PBDRW capture the directional feature of images thus it provides outstanding sparse representation of these features.

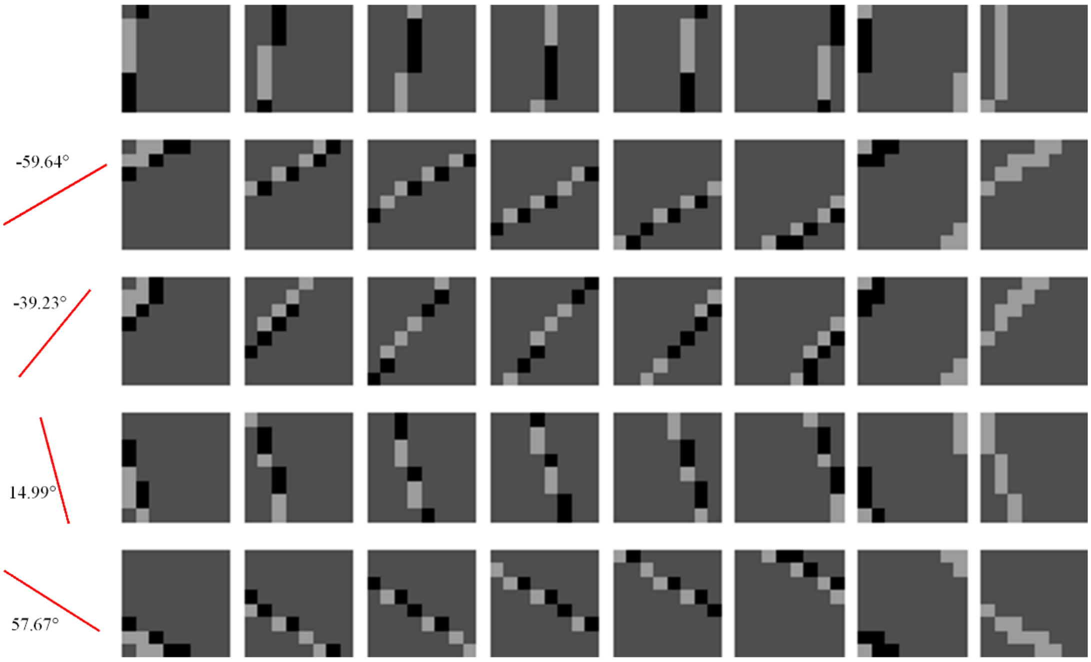

Fig. 2 The basis of PBDRW in 4 directions. Each row shows that 8 basis of PBDRW at a given geometric direction.

2.4 Proposed method

The goal of CS in parallel MRI with NUFFT is to reconstruct a high quality image from highly undersampled k-space data with radial trajectory, thus significantly accelerates MRI. The flowchart of the CS in parallel MRI is summarized in Fig. 3(a). With an object, 8-channel k-space data are partially obtained by sensitivity encoding with the radial trajectory, which is performed on each channel with the same sampling trajectory as shown in Fig. 3(b). With the undersampled k-space data (R is ranging from 2 to 10), a high-resolution image can be reconstructed by the CS-SENSE model. To obtain a reduction factor of R, one in every R interleaves was sampled. All reconstructions are performed on MATLAB with an Intel Core i7-2600 CPU at 3.4 GHz and 16 GB memory.

In numerical simulation, a single channel brain image (size 256×256), shown in Fig. 3(c), is adopted as the object, which is generated from 32 channel full data acquired on a 3T Siemens Trio Tim MRI scanner using the T2-weighted turbo spin echo sequence (TR/TE = 6100/99 ms, FOV=220×220 mm^2, slice thickness=3 mm) [16]. To evaluate the proposed approach, noiseless and simulated eight-channel sensitivity maps of head coils are adopted in the simulation as shown in Fig. 4. The simulation of sensitivity encoding with the radial trajectory is summarized in the dashed rectangle in Fig. 3(a). The sampling matrix = 256×256, number of interleaves = 256.

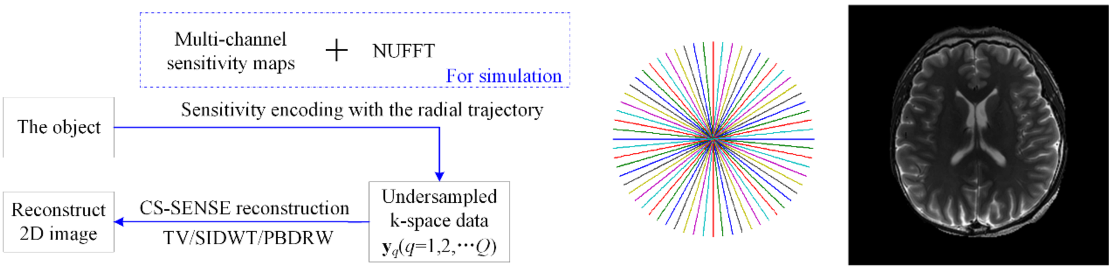

(a) (b) (c)

Fig. 3 The process of the CS in parallel MRI. (a) Flowchart of the CS in parallel MRI; (b) is the radial undersampling trajectory with 32 lines; (c) the high-resolution T2-weighted brain image.

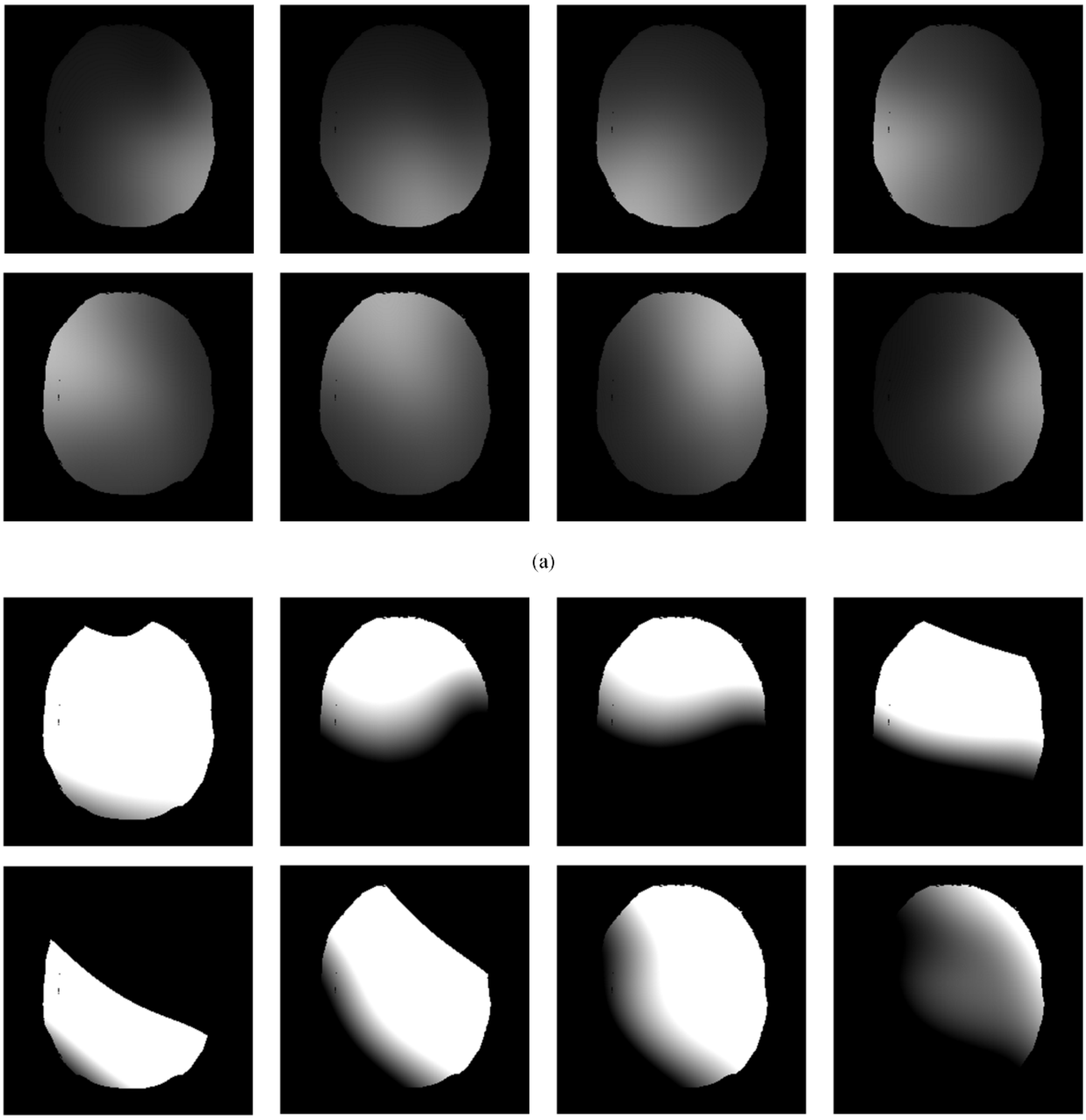

(a)

(b)

Fig. 4 Simulated eight-channel sensitivity maps. (a) magnitude; (b) phase.

For *in vivo* data, the k-space data are acquired from Philips 3T system (Philips Healthcare, Best, The Netherland) using an 8-channel head coil MRI scanner, using T1-weighted fast-field-echo radial sequence with TR/TE = 124/4.5 ms, FOV= 230mm^2, slice thickness = 4mm, acquisition matrix = 656×328, image resolution = 0.70mm^2, number of interleaves = 328.

2.4.1 Reconstruction model

One possible way to apply PBDRW in parallel MRI is combing SENSE and sparse reconstruction as follows:

$$\hat{\mathbf{x}} = \arg\min_{\mathbf{x}} \left\|\mathbf{A}_{\mathbf{W}}\mathbf{x}\right\|_1 + \frac{\lambda}{2}\sum_{q=1}^{Q}\left\|\mathbf{y}_q - \mathbf{F}_{\mathbf{T}}\mathbf{C}_q\mathbf{x}\right\|_2^2 , \tag{2}$$

where $\|\cdot\|_1$ stands for ℓ_1 norm, which indicates a signal is sparse after a known transform $\mathbf{A}_{\mathbf{W}}$, $\|\cdot\|_2$ stands for ℓ_2 norm, which indicates the fidelity of reconstruction, and the parameter λ weighs between the sparsity and data consistency. The notation

$$\mathbf{A}_{\mathbf{w}} = \left[\boldsymbol{\Psi}^T \mathbf{P}(w_1) \mathbf{R}_1 \quad \cdots \quad \boldsymbol{\Psi}^T \mathbf{P}(w_j) \mathbf{R}_j \quad \cdots \quad \boldsymbol{\Psi}^T \mathbf{P}(w_J) \mathbf{R}_J \right]^T \tag{3}$$

stands for the PBDRW forward transform, where $\boldsymbol{\Psi}^T$ is the forward 1D redundant Daubechies wavelet transform, $\mathbf{P}(w_j)$ is an orthogonal operator arranging pixels in each patch parallel to the geometric direction w_j, $\mathbf{R}_j$ is the operation dividing an image $\mathbf{x}$ into patches, and J is the number of patches.

In the CS-SENSE model, coil sensitivity estimation $\mathbf{C}_q$ is critical for the reconstruction performance [3, 38]. The sensitivity maps are assumed to be smooth. Therefore, with pre-Cartesian sampling before the non-uniform sampling in simulation, we use the Cartesian lines at the central of k-space as auto-calibration signal (ACS) to estimate the sensitivity map. Then the sensitivities estimated from ACS lines are smoothed by a Kaiser window with a window shape parameter of 4 [39]. The ACS lines in our experiments are 16 phase encoding lines. With this approach, the estimated sensitivity maps are close to the optimal ones, as shown in Fig. 5(b), when the image backgrounds are removed.

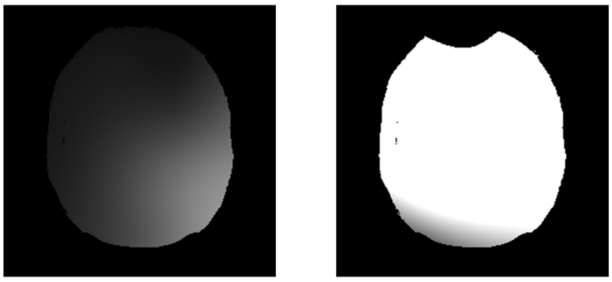

(a)

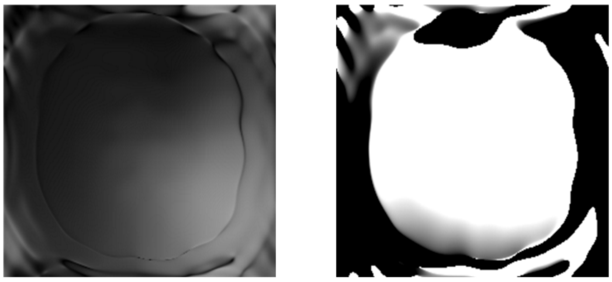

(b)

Fig. 5 Simulated sensitivity map of the first channel. (a) and (b) are estimated from the full scan data and the ACS data, respectively.

2.4.2 Numerical Algorithm

To solve Eq. (2), we follow the alternating direction method with continuation [40], by incorporating an auxiliary variable $\boldsymbol{\alpha}_j = \boldsymbol{\Psi}^T\mathbf{P}(w_j)\mathbf{R}_j\mathbf{x}$ into Eq. (2) according to

$$\min_{\mathbf{x},\boldsymbol{\alpha}_j} \sum_{j=1}^{J}(\|\boldsymbol{\alpha}_j\|_1 + \frac{\beta}{2}\|\boldsymbol{\alpha}_j - \boldsymbol{\Psi}^T\mathbf{P}(w_j)\mathbf{R}_j\mathbf{x}\|_2^2) + \frac{\lambda}{2}\sum_{q=1}^{Q}\|\mathbf{y}_q - \mathbf{F}_\mathbf{T}\mathbf{C}_q\mathbf{x}\|_2^2 . \tag{4}$$

When $\beta \to \infty$ [40], the solution of Eq. (4) approaches that of Eq. (2). In implementation, β will be increased by a factor of 2. A solution for a smaller β will be used as a warm start for solving optimization problem with a larger β [41]. When β is fixed, we solve Eq. (4) as follows:

(1) Fixing $\mathbf{x}$, solve $\boldsymbol{\alpha}_j$ via soft threshold:

$$\boldsymbol{\alpha}_j = \max(|\boldsymbol{\Psi}^T\mathbf{P}(w_j)\mathbf{R}_j\mathbf{x}| - \frac{1}{\beta}, 0)\frac{\boldsymbol{\Psi}^T\mathbf{P}(w_j)\mathbf{R}_j\mathbf{x}}{|\boldsymbol{\Psi}^T\mathbf{P}(w_j)\mathbf{R}_j\mathbf{x}|} ; \tag{5}$$

(2) Fixing all the $\boldsymbol{\alpha}_j\,(j = 1,\cdots,J)$, solve $\mathbf{x}$ according to

$$\min_{\mathbf{x}} \sum_{j=1}^{J}(\frac{\beta}{2}\|\boldsymbol{\alpha}_j - \boldsymbol{\Psi}^T\mathbf{P}(w_j)\mathbf{R}_j\mathbf{x}\|_2^2) + \frac{\lambda}{2}\sum_{q=1}^{Q}\|\mathbf{y}_q - \mathbf{F}_\mathbf{T}\mathbf{C}_q\mathbf{x}\|_2^2 ; \tag{6}$$

One has

$$\beta\sum_{j=1}^{J}\mathbf{R}_j^T\mathbf{P}^T(w_j)\boldsymbol{\Psi}\boldsymbol{\Psi}^T\mathbf{P}(w_j)\mathbf{R}_j\mathbf{x} + \lambda\sum_{q=1}^{Q}\mathbf{C}_q^H\mathbf{F}_T^H\mathbf{F}_T\mathbf{C}_q\mathbf{x} = \beta\sum_{j=1}^{J}\mathbf{R}_j^T\mathbf{P}^T(w_j)\boldsymbol{\Psi}\boldsymbol{\alpha}_j + \lambda\sum_{q=1}^{Q}\mathbf{C}_q^H\mathbf{F}_T^H\mathbf{y}_q , \tag{7}$$

where $e\mathbf{I} = \sum_{j=1}^{J}\mathbf{R}_j^T\mathbf{R}_j$; $\mathbf{I}$ is a unit matrix; the superscript 'H' means Hermitian transpose of a matrix; and e is overlapping factor of image patches, which is defined as $e = \frac{G}{l^2}$ [19], where $\sqrt{G}$ the side length of a square patch and l is the sliding distance. In this paper, e is 4 since $\sqrt{G} = 8$ and $l = 4$ [19].

Since $\boldsymbol{\Psi}\boldsymbol{\Psi}^T = \kappa\mathbf{I}$ (κ is the redundancy degree, which is 4 for all experiments in this paper), $\mathbf{P}^T(w_j)\mathbf{P} = \mathbf{I}$, the solution of Eq. (7) is

$$(\beta e\kappa\mathbf{I} + \lambda\sum_{q=1}^{Q}\mathbf{C}_q^H\mathbf{F}_\mathbf{T}{}^H\mathbf{F}_\mathbf{T}\mathbf{C}_q)\mathbf{x} = \beta\mathbf{S}_\alpha + \lambda\sum_{q=1}^{Q}\mathbf{C}_q^H\mathbf{F}_\mathbf{T}{}^H\mathbf{y}_q \tag{8}$$

where $\mathbf{S}_\alpha = \sum_{j=1}^{J}\mathbf{R}_j^T\mathbf{P}^T(w_j)\boldsymbol{\Psi}\boldsymbol{\alpha}_j$. Finally, Eq. (8) is solved according to

$$\mathbf{A}\mathbf{x} = \mathbf{b} \tag{9}$$

using the preconditioned conjugate gradient method.

Table 1 Algorithm for PBDRW-based CS SENSE reconstruction.

```
Initialization:
Input the acquired multichannel k-space data $\mathbf{y}_q$, the estimated sensitivity map $\mathbf{C}_q$, the geometric directions $\mathbf{P}_j\{j=1,\cdots,\mathrm{J}\}$ of $j^{\text{th}}$ patch and overlap factor $e$, the undersampled non-uniform fast Fourier operator $\mathbf{F}_T$, the redundant Daubechies wavelet transform $\mathbf{\Psi}$ and redundancy $\kappa$, the regularization parameter $\lambda$ and tolerance of inner loop $\varepsilon=5\times10^{-4}$.
Initialize $\mathbf{x}=\sum_q \mathbf{F}_T^H \mathbf{y}_q$, $\mathbf{x}_{last}=\mathbf{x}$, $\beta=2^8$ and $\alpha_j=0$ for all $j=1,\cdots,\mathrm{J}$

Main:
  While $\beta\le 2^{16}$
    (1) For $j=1,\cdots,\mathrm{J}$: Given $\mathbf{x}$, solve Eq. (5) and obtain the solution $\boldsymbol{\alpha}_j\left(j=1,\cdots,J\right)$.
    (2) Given $\boldsymbol{\alpha}_j\left(j=1,\cdots,J\right)$, solve Eq. (8) and obtain the solution $\mathbf{x}$;
    (3) If $\|\Delta\mathbf{x}\|=\|\mathbf{x}_{last}-\mathbf{x}\|>\varepsilon$, then $\mathbf{x}_{last}\leftarrow\mathbf{x}$, go to step (1);
        Otherwise, go to step (4);
    (4) $\hat{\mathbf{x}}\leftarrow\mathbf{x}$, $\beta\leftarrow 2\beta$, go to step (1);
  End while
Output $\hat{\mathbf{x}}$
```

3. Results

In this section, we compare different reconstruction methods on simulated and *in vivo* data. TV and SIDWT are selected to be compared since TV is typically used in PPI [30, 42] and SIDWT a typical sparsifying transform in CS-MRI[16]. $\mathbf{A}_{\mathbf{w}}$ is replaced with SIDWT or TV operator in Eq. (2). As it is mentioned before, the image reconstructed using SIDWT will provide the initial geometric directions for PBDRW.

The reconstruction error, relative ℓ_2 norm error (RLNE), defined as

$$\mathrm{RLNE}\left(\hat{\mathbf{x}}\right)=\frac{\|\hat{\mathbf{x}}-\tilde{\mathbf{x}}\|_2}{\|\tilde{\mathbf{x}}\|_2}, \tag{10}$$

is used to measure the difference between the reconstructed image $\hat{\mathbf{x}}$ and groundtruth (fully sampled and noiseless) image $\tilde{\mathbf{x}}$ [19, 36].

The signal-to-noise ratio (SNR) is measured on the image according to

$$\mathrm{SNR}_{\mathrm{dB}} = 10\log_{10}\left(\frac{u}{\sigma}\right), \tag{11}$$

where u is the mean of image intensity and σ is the standard deviation of noise in the image background.

Structural similarity (SSIM) [3] measures the similarity of two local images in a window. The SSIM value of two windows are attribute to the central pixel in that window. Hence, the SSIM is a function of $\tilde{x}_i$ and $\hat{x}_i$, which are the center of local images **a** and **b** with a window size of $G\times G$ (G is 8 in this paper).

The SSIM is defined as

$$\mathrm{SSIM}(\tilde{x}_i, \hat{x}_i) = \mathrm{SSIM}(\mathbf{a},\mathbf{b}) = \frac{\left(2u_a u_b + E_1\right)\left(2\sigma_{ab} + E_2\right)}{\left(u_a^2 + u_b^2 + E_1\right)\left(\sigma_a^2 + \sigma_b^2 + E_2\right)} \tag{12}$$

where u_a is the average of **a**, u_b is the average of **b**, σ_a is the standard deviation of **a**, σ_b is the standard deviation of **b**, σ_{ab} is the covariance of **a** and **b**, E_1 and E_2 are two variables to stabilize the division with weak denominator.

According to the definition in Eq. (2), the SSIM is a function of central pixels $\tilde{x}_i$ and $\hat{x}_i$. For a whole image, we use the mean SSIM (MSSIM) to evaluate the preserved structures in reconstruction. The MSSIM is defined as:

$$\mathrm{MSSIM}(\tilde{\mathbf{x}}, \hat{\mathbf{x}}) = \frac{1}{T}\sum_i \mathrm{SSIM}(\tilde{x}_i, \hat{x}_i), \tag{13}$$

where $\tilde{\mathbf{x}}$ and $\hat{\mathbf{x}}$ are the groundtruth image and the reconstructed image, respectively, $\tilde{x}_i$ and $\hat{x}_i$ are the corresponding center of local images at the i^{th} local window, and T is the number of total local windows that is equal to the number of image pixels.

3.1 Numerical Simulation

In simulated reconstruction, the partially sampled k-space data (R=8) on radial trajectory are obtained using NUFFT on simulated channel images, and then Gaussian white noises are added to the k-space data in the real and imaginary parts, respectively. The noise standard deviation is 0.01 in simulation. The global evaluation criteria for reconstructed images are listed in Tables 2 and reconstructed images are shown in Fig. 6.

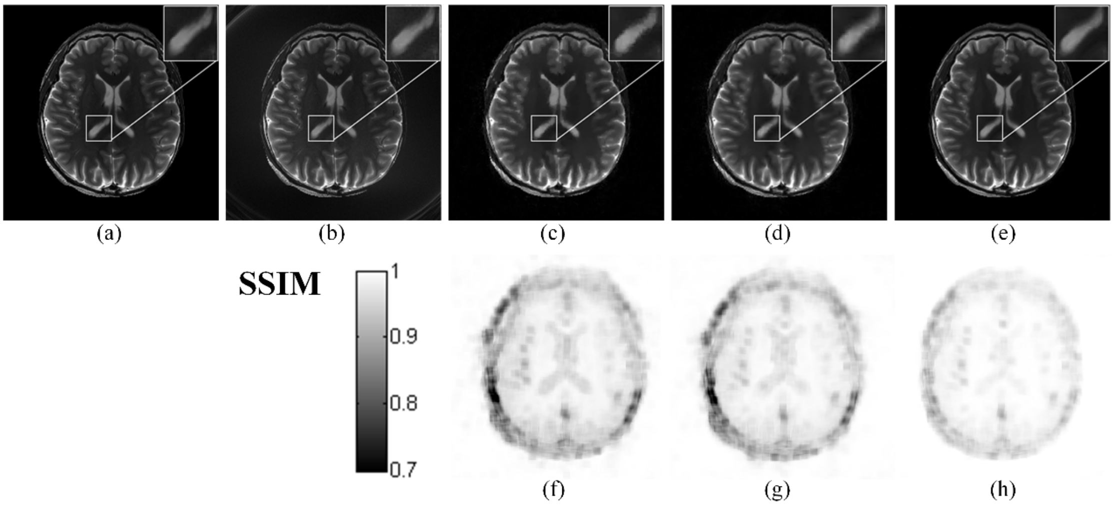

Fig. 6 Reconstructed images and SSIMs from radial undersampling data with low added artificial noise. (a) is the groundtruth image; (b) the full sampled image for noise-added data; (c)-(e) are reconstructed images using TV, SIDWT, PBDRW while (f)-(h) are the SSIMs corresponding to (c)-(e), respectively.

Table 2 Evaluation criteria with low noise-added undersampling data.

Methods	Images	Evaluation criteria			Regularization parameter
		RLNE	MSSIM	SNR(dB)	
TV	Fig. 6(c)	0.1913	0.9932	16.65	2×10^3
SIDWT	Fig. 6(d)	0.1759	0.9934	16.98	1×10^3
PBDRW	Fig. 6(e)	0.1128	0.9974	18.95	5×10^4

Note: 32 radial lines (R=8) are used for reconstruction.

The proposed method achieves lower reconstruction error than other methods. The Table 2 shows that the PBDRW achieves the lowest RLNE, highest MSSIM and SNR among all three methods. This is consistent to the observation that PBDRW preserve more image details and structures as shown in Figs. 6. The enlarged area of Figs. 6(c)-(e) imply that the PBDRW achieves better resolution than TV and SIDWT. Besides, the Figs. 6(f)-(h) obviously show that the higher SSIMs are achieved in most regions using PBDRW than other two methods.

3.2 *In vivo* data reconstruction

In this section, RLNEs and MSSIMs are not used since ground truth (fully sampled and noiseless) data are not available. We also verify the performance of three methods in two slices, and the reconstructed images for R=6 are shown in Fig.7. The results show that the proposed method leads to sharper edges in reconstructed images. Therefore, the proposed method obtains higher fidelity to the fully sampled image than other methods.

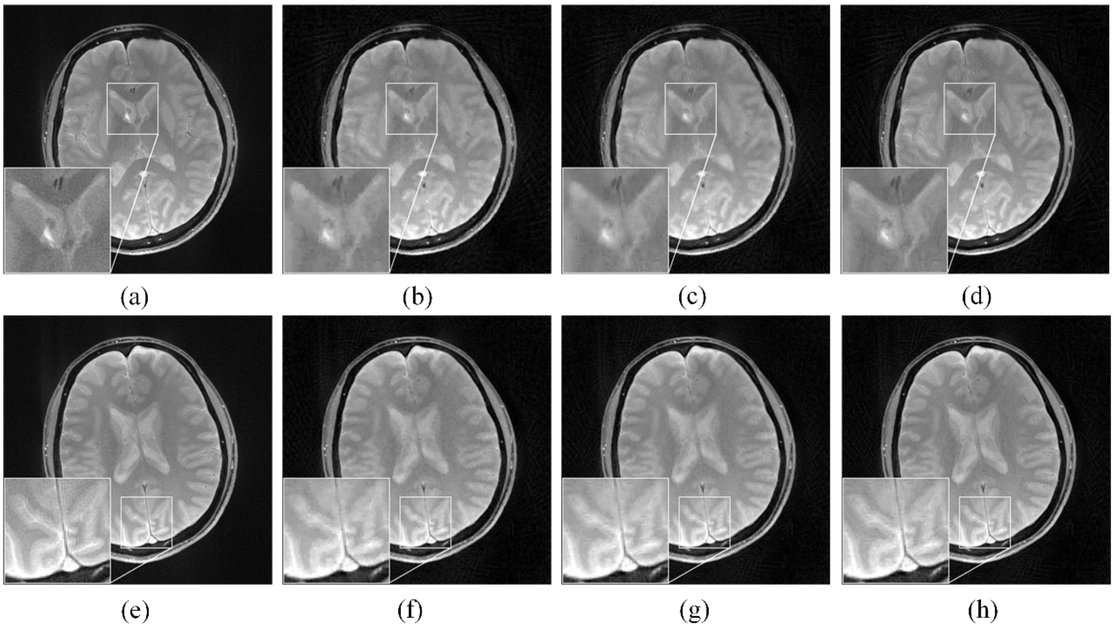

Fig. 7 Reconstructed images for two slices of in vivo data. Left to right: The SOS of fully sampled channel images; reconstructed images using TV, SIDWT, PBDRW.

4. Discussions

4.1 Different reduction factor R

In simulation, different reduction factors are adopted to the k-space data present in Section 3.1. The performance of reconstruction using three methods are evaluated in Figs. 8. When reduction factor is from 2 to 10, the consistent reduction of reconstruction error using PBDRW is always lowest among three methods. Besides, these MSSIMs indicate the reconstructed image using PBDRW is most similar structure to the groundtruth image. However, the SNR index using PBDRW is not consistent with RLNE under different reduction factors (Fig. 8(c)). This is because that an optimal parameter λ, achieving the lowest RLNE, may not lead to a highest SNR. Figs. 9(d1)-(d3) show that reconstructed images preserve sharper edges when more data are sampled although the SNR is decreased. These observations show that the proposed method always hold better reconstruction at different reduction factors.

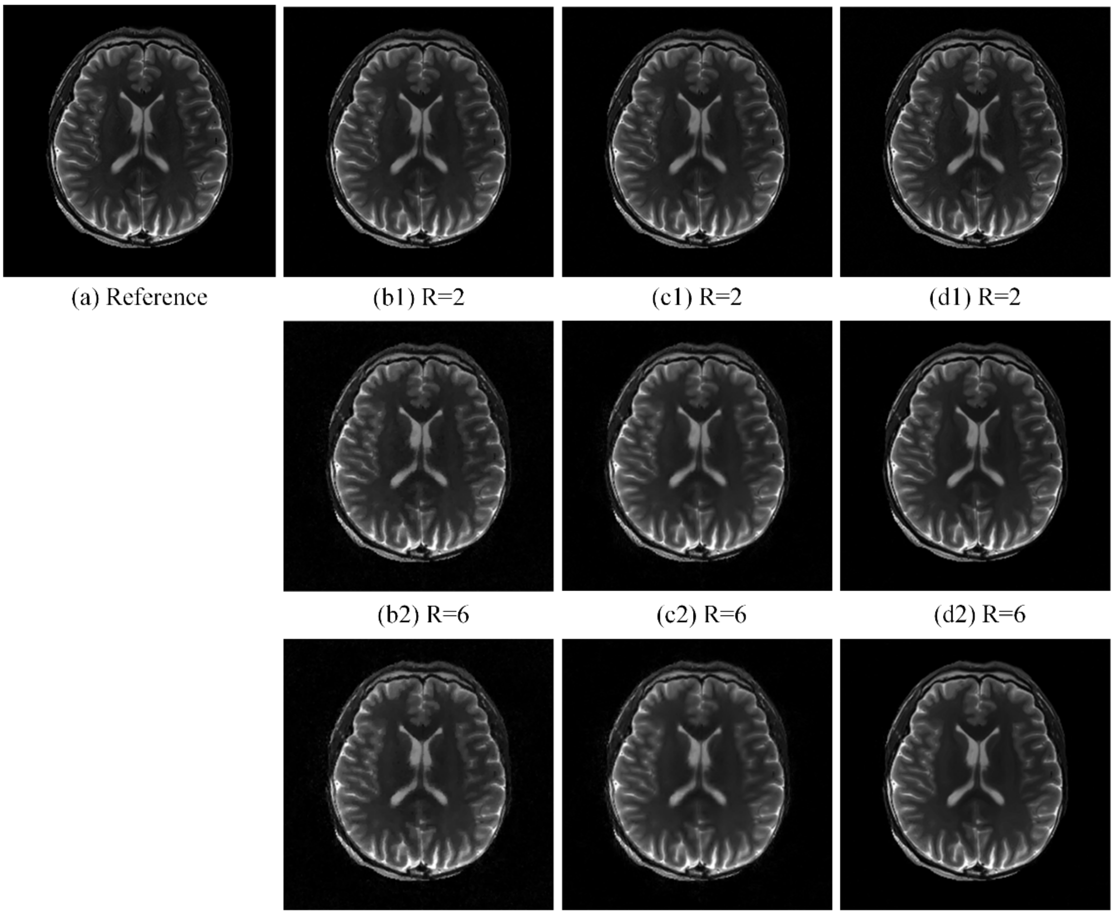
(a) Reference (b1) R=2 (c1) R=2 (d1) R=2

(b2) R=6 (c2) R=6 (d2) R=6

(b3) R=8 (c3) R=8 (d3) R=8

Fig. 9 Reconstructed images under different reduction factors using TV (b1-b3), SIDWT (c1-c3) and PBDRW (d1-d3), respectively.

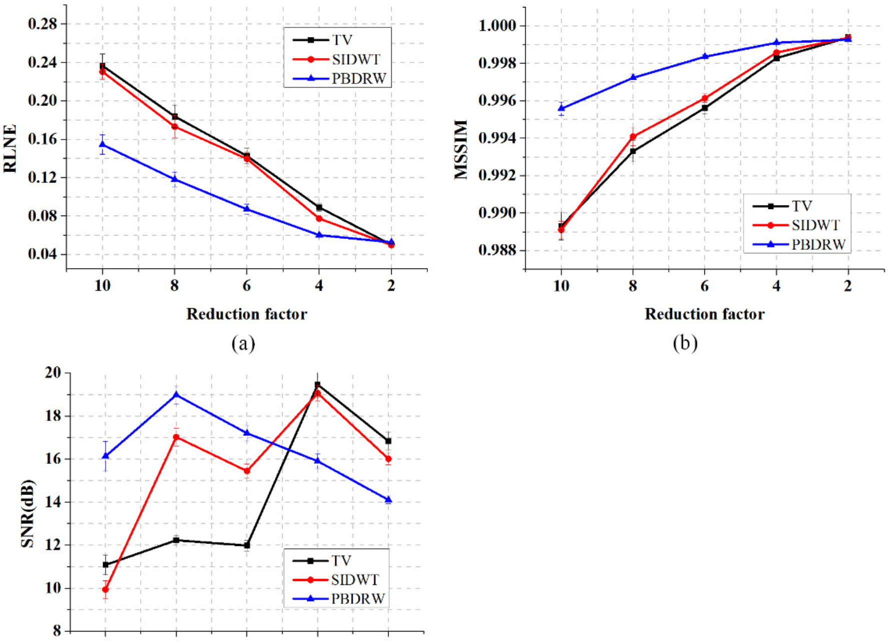

(a)

(b)

(c)

Fig. 8 Evaluation criteria for reconstructed image under different reduction factors. (a)-(c) are RLNEs, MSSIMs and SNRs respectively.

4.2 Reconstruction with PBDRW versus PBDW

To investigate the use of the redundant-wavelets-based PBDRW for image reconstruction, we choose the orthogonal-wavelets-based PBDW to be compared. In simulation, the Gaussian white noise, with standard deviation 0.01, is added to the radial undersampling data (R=10). The evaluation criteria are listed in Table 3 and reconstructed images are shown in Fig. 10. In comparison, the evaluation criteria using PBDRW and PBDW are comparable, but the SSIMs using PBDRW in the region (as red marked in Figs. 10) is higher than using PBDW. Besides, the PBDRW achieves more smooth edges than PBDW, as zoomed in Figs. 10(d) and (e). Thus, the PBDRW performs smoother image than the PBDW.

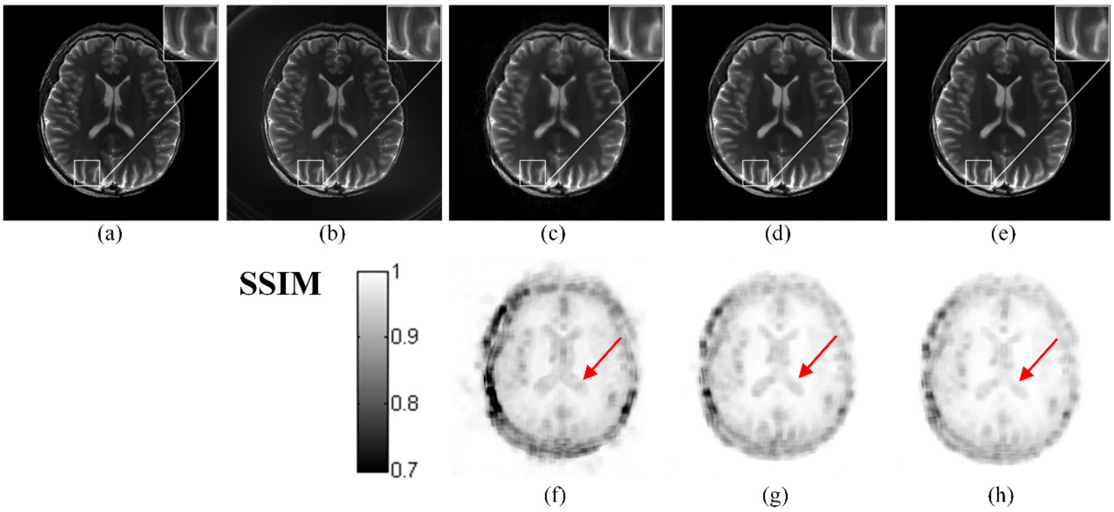

Fig. 10 Reconstructed images and SSIMs using SIDWT, PBDW and PBDRW. (a) is the groundtruth image; (b) the full sampled image for noise-added data; (c)-(e) are reconstructed images using SIDWT, PBDW and PBDRW while the direction estimated from (c); (f)-(h) are the SSIMs corresponding to (c)-(e), respectively.

Table 3 Evaluation criteria using the methods of SIDWT, PBDW and PBDRW.

Methods	Images	Evaluation criteria			Regularization parameter
		RLNE	MSSIM	SNR(dB)	
SIDWT	Fig. 10(c)	0.2323	0.9901	16.99	1×10^3
PBDW	Fig. 10(d)	0.1872	0.9942	19.51	5×10^4

PBDRW	Fig. 10(e)	0.1707	0.9950	20.04	5×10^4

Note: 26 radial lines (R=10) are used for reconstruction.

4.3 Reconstruction with larger added noise in k-space

In Section 3, the proposed method outperforms other methods with the low noise. Nevertheless, it is unknown whether the advantage of the proposed method will be lost for a larger noise. In this section, the added Gaussian white noise standard deviation is raised to 0.02 in simulation. The evaluation criteria are listed in Table 4 and reconstructed images are shown in Fig. 11. For a greater noise level, the proposed method preserves more image edges than other methods although the advantage of denoising using PBDRW is lost. The PBDRW can still achieve lowest RLNE and highest MSSIM, but the SNR using PBDRW will be comparable to using the other method. Furthermore, the computational time of the proposed method is longer than using SIDWT and comparable to using TV. The Figs. 11(e) and (h) firmly show that PBDRW still produces obviously sharper edges and lose minimal image structures than the other methods.

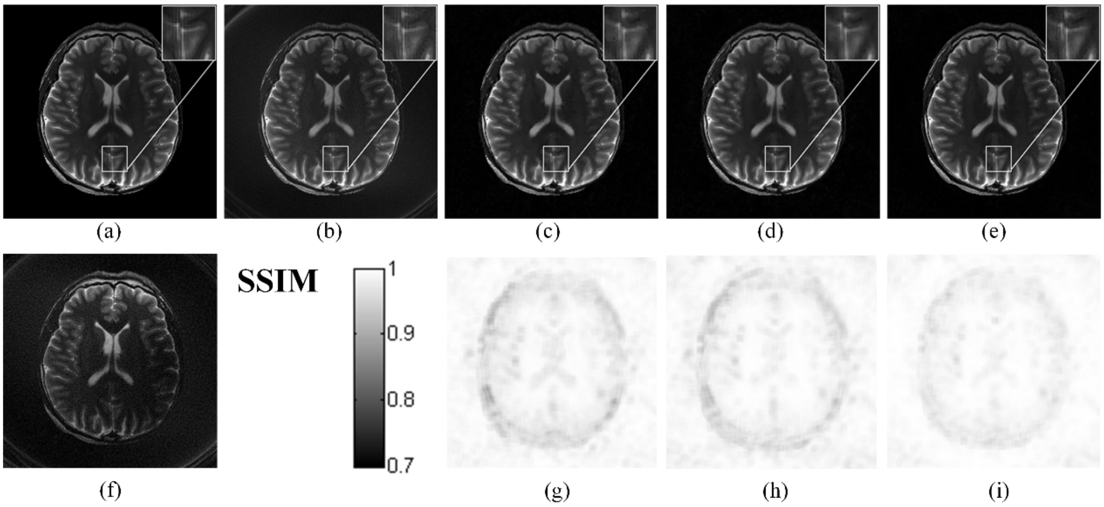

Fig. 11 Reconstructed images and SSIMs with larger added noise. (a) is the groundtruth image; (b) the full sampled SOS image for noise-added data while (f) is one of eight-channel images; (c)-(e) are reconstructed images using TV, SIDWT, PBDRW while (g)-(h) are the SSIMs corresponding to (c)-(e), respectively.

Table 4 Evaluation criteria with lager noise-added undersampling data.

Methods	Images	Evaluation criteria			Regularization parameter	Computational time (s)
		RLNE	MSSIM	SNR(dB)		

TV	Fig. 11(c)	0.1334	0.9961	11.71	1×10^3	404
SIDWT	Fig. 11(d)	0.1217	0.9963	11.44	5×10^2	112
PBDRW	Fig. 11(e)	0.0979	0.9976	11.65	3×10^4	349

Note: 64 radial lines (R=4) are used for reconstruction.

4.4 Reconstruction with CS-MRI followed by SOS

The regularization of CS-SENSE occurs only in the target image based on the original image is sparse or compressible in image domain or wavelet domain. However, the target image can also be reconstructed by a simple model without sensitivity estimation if the multi-channel images are still sparse in same transform. The target image is obtained by the SOS of all channel images, and the "SOS" means Sum of Square (SOS), defined as $\tilde{\mathbf{x}} = \sqrt{\frac{1}{Q}\sum_{q=1}^{Q}\left(\mathbf{x}_i\right)^2}$, where $\mathbf{x}_i$ is the single-channel image and the total number of channels is Q [19] (CS-MRI-SOS).

In simulated reconstruction, the radial sampling k-space data without added noise are used. In comparison, the proposed method achieves lower reconstruction error and higher MSSIM in Table 5 than the CS-MRI-SOS, and the PBDRW achieves lowest reconstruction error among three transforms in the CS-MRI-SOS. With limited data, the CS-MRI-SOS images are more blurry than the CS-SENSE one although the PBDRW achieves sharpest image edges in the CS-MRI-SOS, as shown in Fig 12. The Figs. 12(f)-(i) obviously show that the proposed method preserves more image structures than other methods.

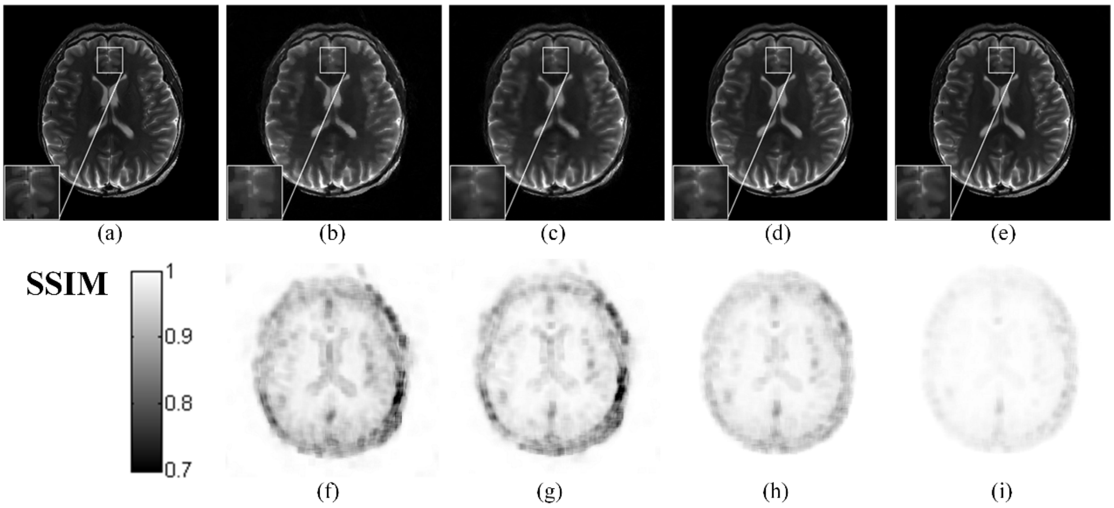

Fig. 12 Reconstructed images and SSIMs with different methods. (a) is the groundtruth image; (b)-(d) are reconstructed images using TV, SIDWT, PBDRW from CS-MRI-SOS, while (e) is reconstructed from the proposed method with directions estimated from (c); (f)-(i) are SSIMs, corresponding.

Table 5 Evaluation criteria with noiseless undersampling data.

Methods	Images	Evaluation criteria		Regularization parameter
		RLNE	MSSIM	
TV in CS-MRI-SOS	Fig. 12(b)	0.2143	0.9917	1×10^5
SIDWT in CS-MRI-SOS	Fig. 12(c)	0.1761	0.9934	1×10^6
PBDRW in CS-MRI-SOS	Fig. 12(d)	0.1489	0.9960	1×10^6
PBDRW in CS-SENSE	Fig. 12(e)	0.0855	0.9986	1×10^6

Note: 32 radial lines (R=8) are used for reconstruction.

4.5 Reconstruction with CS-MRI using DL, PANO and PBDRW

In this section, we compare the proposed PBDRW to dictionary learning (DL) [44] and the patch-based nonlocal operator (PANO) [36] for CS-MRI reconstruction. Since both the DL and PANO are originally applied into single channel MRI reconstruction, and revise these methods to fit for parallel imaging is hard, we only compare the results on single channel imaging. Extension of DL and PANO in to parallel imaging will be of great interest and we plan to do it in the future. In simulation, the Cartesian sampling pattern (Fig. 13(e)) is adopted in undersampling. As shown in Table 6, the RLNE and MSSIM indexes of PBDRW and PANO are comparable and both of them are better than that of DL-based CS-MRI. Figs. 13(a)-(d) indicate that the edges of reconstruction images using PBDRW and PANO are better preserved than that using DL, which is consistent to the observation in Figs. 13(f)-(g).

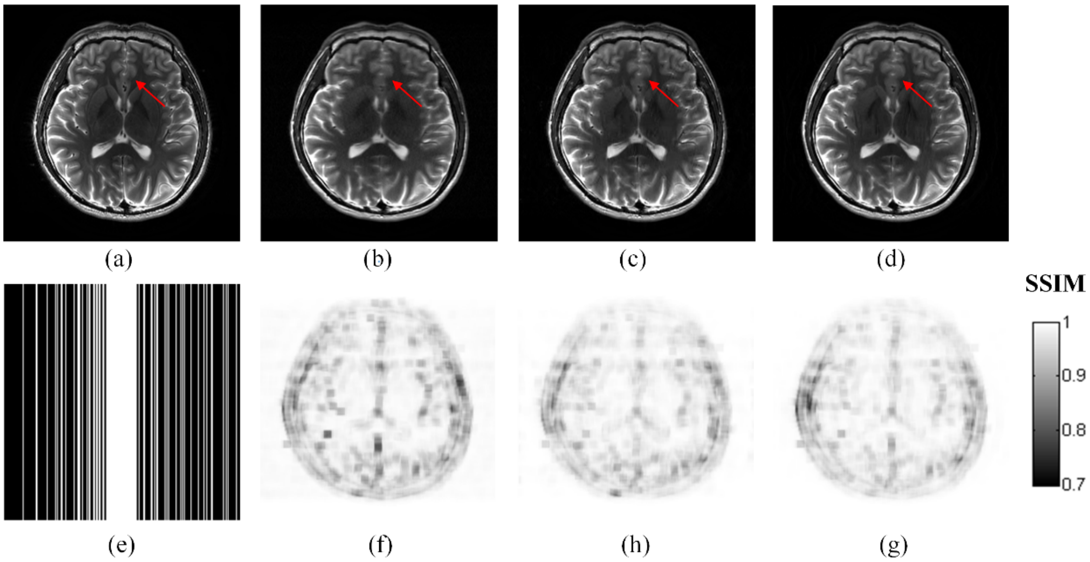

Fig. 13 The reconstructed images and SSIMs with CS-MRI. (a) the ground truth image; (b)-(d) are reconstructed images using dictionary learning (DL), PANO, and PBDRW, while (f)-(h) are corresponding SSIMs; (e) is the sampling pattern.

Table 6 Evaluation criteria with Cartesian undersampling data in CS-MRI.

Methods	Images	Evaluation criteria		Parameters	Computational time (s)
		RLNE	MSSIM		
DL	Fig. 13(b)	0.1236	0.9939	K2 = 32*n; num = 25; n = 64.	2.40×10^4
PANO	Fig. 13(c)	0.0956	0.9954	$\lambda = 1\times10^6$	1.30×10^2
PBDRW	Fig. 13(d)	0.1069	0.9956	$\lambda = 1\times10^6$	2.72×10^3

Note: 32% of fully sampled k-space data in Fig. 13(a) is used for reconstruction.

4.6 Convergence of the algorithm

The proof of the convergence of the algorithm proposed in this paper is similar to the one given in [45]. The empirical convergence result of the algorithm is shown in Fig. 14. It shows that the objective function decreases gradually and finally stabilizes. For the Preconditioning Conjugate Gradient (PCG) step, the algorithm achieves fully converged before 10 iterations, which means the norm of solution difference in two consecutive iterations is lower than 10^{-6}. PCG is considered to converge under this level of difference. Since the computation step is not time consuming, we suggest users to make sure PCG converge.

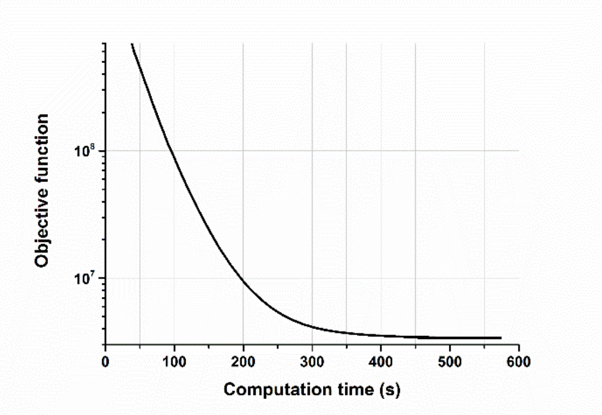

Fig. 14 Empirical convergence of the objective function. Note: The k-space data of in Section 3.1 is used for this experiment.

4.7 Regularization parameters

How to choose the regularization parameters λ is discussed in this section. The regularization parameter λ is chosen to achieve the lowest reconstruction errors. Ideally, λ can be as large as possible if the data are free of noise. But with the noisy data, regularization parameter λ is crucial to minimize reconstruction errors since a smaller λ penalizes the noise more heavily and a larger λ preserves more image structures. The influence of λ on the reconstruction error is studied in Fig. 15. A smaller λ leads to a higher RLNE and SNR, while a larger λ leads to a higher RLNE and lower SNR. The reconstructed images using different λ are shown in Fig. 16. It shows that a too small λ leads to an over-smoothed image while a too large λ will introduce obvious noise. In experiments, the optimal λ lies in the range from 2×10^4 to 8×10^4.

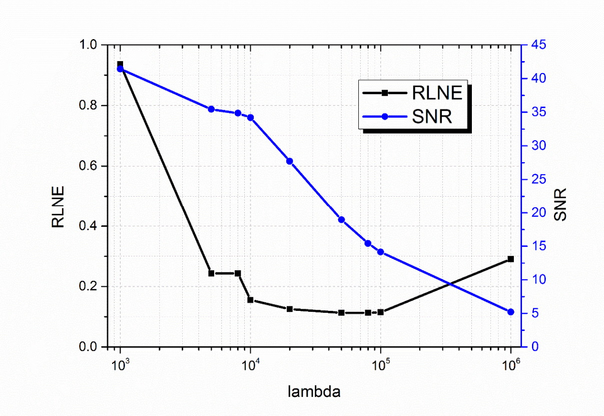

Fig. 15 Effects of regularization parameter λ for image reconstruction from noisy data.

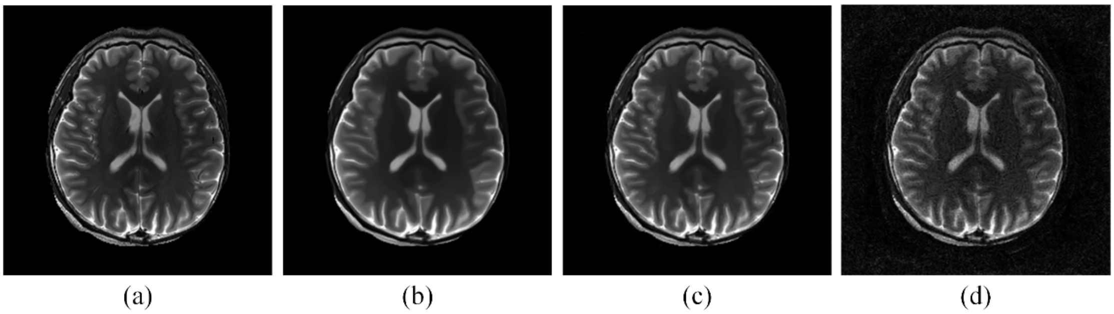

Fig. 16 Reconstructed images under different regularization parameter λ. (a) the ground-truth image; (b)-(d) are reconstructed images using $\lambda=10^4$, 5×10^4 and $\lambda=10^6$, respectively.

5. Conclusion

In this paper, the patch-based directional redundant wavelets (PBDRW) is introduced into parallel MRI reconstruction for radial sampling in a compressed sensing SENSE model. Results on simulated and *in vivo* data show that the proposed method better preserves image edges than traditional CS-MRI methods based on total variation and shift-invariant discrete wavelets. The advantage of PBDRW in providing a sparser representation of image patch with edges still holds when non-uniform fast Fourier transform is applied. With a relatively low noise level, the proposed method achieves a higher SNR and MSSIM than other methods. However, when the noise standard deviation is increased to 0.02, the SNR advantage is not obvious although edge is still better preserved by PBDRW. Therefore, how to preserve the image edges in reconstructions under high noises is still open.

Conflict of Interests

The authors declare that there is no conflict of interests regarding the publication of this paper.

Acknowledgements

The simulated eight-channel sensitivity maps of head coils are made by Dr. Feng Huang at Philips Company. This work was supported by the NNSF of China (61201045, 11375147 and 61302174), Natural Science Foundation of Fujian Province of China (No. 2015J01346), Important Joint Research Project on Major Diseases of Xiamen City (3502Z20149032), Open Fund from Key Lab of Digital Signal and Image Processing of Guangdong Province (2013GDDSIPL-07) and Scientific Research Foundation for the Introduction of Talent at Xiamen University of Technology (YKJ12021R).

References

[1] K. P. Pruessmann, M. Weiger, M. B. Scheidegger, and P. Boesiger, SENSE: Sensitivity encoding for fast MRI, Magn Reson

Med, 42, 952-962 **(1999)**.

[2] W. E. Kyriakos, L. P. Panych, D. F. Kacher, C.-F. Westin, S. M. Bao, R. V. Mulkern, and F. A. Jolesz, Sensitivity profiles from an array of coils for encoding and reconstruction in parallel (SPACE RIP), Magn Reson Med, 44, 301-308 **(2000)**.

[3] A. Majumdar and R. K. Ward, Calibration-less multi-coil MR image reconstruction, Magn Reson Imaging, 30, 1032-1045 **(2012)**.

[4] S. Feng, Y. Zhu, and J. Ji, Efficient large-array k-domain parallel MRI using channel-by-channel array reduction, Magn Reson Imaging, 29, 209-215 **(2011)**.

[5] A. G. Christodoulou, H. Zhang, B. Zhao, T. K. Hitchens, C. Ho, and Z. P. Liang, High-resolution cardiovascular MRI by integrating parallel imaging with low-rank and sparse modeling, IEEE Trans Biomed Eng, 60, 3083-3092 **(2013)**.

[6] D. K. Sodickson and W. J. Manning, Simultaneous acquisition of spatial harmonics (SMASH): Fast imaging with radiofrequency coil arrays, Magn Reson Med, 38, 591-603 **(1997)**.

[7] M. A. Griswold, P. M. Jakob, Q. Chen, J. W. Goldfarb, W. J. Manning, R. R. Edelman, and D. K. Sodickson, Resolution enhancement in single-shot imaging using simultaneous acquisition of spatial harmonics (SMASH), Magn Reson Med, 41, 1236-1245 **(1999)**.

[8] M. A. Griswold, P. M. Jakob, R. M. Heidemann, M. Nittka, V. Jellus, J. Wang, B. Kiefer, and A. Haase, Generalized autocalibrating partially parallel acquisitions (GRAPPA), Magn Reson Med, 47, 1202-1210 **(2002)**.

[9] L. Xu, Y. Feng, X. Liu, L. Kang, and W. Chen, Robust GRAPPA reconstruction using sparse multi-kernel learning with least squares support vector regression, Magn Reson Imaging, 32, 91-101 **(2014)**.

[10] J. Miao, W. Guo, S. Narayan, and D. L. Wilson, A simple application of compressed sensing to further accelerate partially parallel imaging, Magn Reson Imaging, 31, 75-85 **(2013)**.

[11] M. Lustig and J. M. Pauly, SPIRiT: Iterative self-consistent parallel imaging reconstruction from arbitrary k-space, Magn Reson Med, 64, 457-471 **(2010)**.

[12] Z. Feng, F. Liu, M. F. Jiang, S. Crozier, H. Guo, and Y. X. Wang, Improved L1-SPIRiT using 3D walsh transform-based sparsity basis, Magn Reson Imaging, 32, 924-933 **(2014)**.

[13] A. Majumdar and R. K. Ward, Nuclear norm-regularized SENSE reconstruction, Magn Reson Imaging, 30, 213-221 **(2012)**.

[14] G. X. Xie, Y. B. Song, C. Y. Shi, X. Feng, H. R. Zheng, D. H. Weng, B. S. Qiu, and X. Liu, Accelerated magnetic resonance imaging using the sparsity of multi-channel coil images, Magn Reson Imaging, 32, 175-183 **(2014)**.

[15] M. F. Jiang, J. Jin, F. Liu, Y. Y. Yu, L. Xia, Y. M. Wang, and S. Crozier, Sparsity-constrained SENSE reconstruction: An efficient implementation using a fast composite splitting algorithm, Magn Reson Imaging, 31, 1218-1227 **(2013)**.

[16] M. Lustig, D. Donoho, and J. M. Pauly, Sparse MRI: The application of compressed sensing for rapid MR imaging, Magn Reson Med, 58, 1182-1195 **(2007)**.

[17] C. H. Chang and J. Ji, Compressed sensing MRI with multichannel data using multicore processors, Magn Reson Med, 64, 1135-1139 **(2010)**.

[18] B. Zhao, J. P. Haldar, A. G. Christodoulou, and Z. P. Liang, Image reconstruction from highly undersampled (k, t) -space data with joint partial separability and sparsity constraints, IEEE Trans Med Imaging, 31, 1809-1820 **(2012)**.

[19] X. B. Qu, D. Guo, B. D. Ning, Y. K. Hou, Y. L. Lin, S. H. Cai, and Z. Chen, Undersampled MRI reconstruction with patch-based directional wavelets, Magn Reson Imaging, 30, 964-977 **(2012)**.

[20] D. C. Peters, P. Rohatgi, R. M. Botnar, S. B. Yeon, K. V. Kissinger, and W. J. Manning, Characterizing radial undersampling artifacts for cardiac applications, Magn Reson Med, 55, 396-403 **(2006)**.

[21] K. L. Wright, J. I. Hamilton, M. A. Griswold, V. Gulani, and N. Seiberlich, Non-Cartesian parallel imaging reconstruction, Magn Reson Imaging, 1-19 **(2014)**.

[22] R. M. Heidemann, M. A. Griswold, N. Seiberlich, G. Krüger, S. A. R. Kannengiesser, B. Kiefer, G. Wiggins, L. L. Wald, and P. M. Jakob, Direct parallel image reconstructions for spiral trajectories using GRAPPA, Magn Reson Med, 56, 317-326 **(2006)**.

[23] F. Knoll, G. Schultz, K. Bredies, D. Gallichan, M. Zaitsev, J. Hennig, and R. Stollberger, Reconstruction of undersampled radial PatLoc imaging using total generalized variation, Magn Reson Med, 70, 40-52 **(2013)**.

[24] S. Kashyap, Z. L. Yang, and M. Jacob, Non-iterative regularized reconstruction algorithm for non-Cartesian MRI: NIRVANA, Magn Reson Imaging, 29, 222-229 **(2011)**.

[25] H. K. Song and L. Dougherty, K-space weighted image contrast (KWIC) for contrast manipulation in projection reconstruction MRI, Magn Reson Med, 44, 825-832 **(2000)**.

[26] M. I. Altbach, E. K. Outwater, T. P. Trouard, E. A. Krupinski, R. J. Theilmann, A. T. Stopeck, M. Kono, and A. F. Gmitro, Radial fast spin-echo method for T2-weighted imaging and T2 mapping of the liver, J Magn Reson Imaging, 16, 179-189 **(2002)**.

[27] A. Dutt and V. Rokhlin, Fast Fourier transforms for nonequispaced data, SIAM J. Sci. Comput., 14, 1368-1393 **(1993)**.

[28] C. W. Hu, X. B. Qu, D. Guo, L. J. Bao, and Z. Chen, Wavelet-based edge correlation incorporated iterative reconstruction for undersampled MRI, Magn Reson Imaging, 29, 907-915 **(2011)**.

[29] E. Le Pennec and S. Mallat, Sparse geometric image representations with bandelets, IEEE Trans Image Process, 14, 423-438 **(2005)**.

[30] F. Huang, Y. Chen, W. Yin, W. Lin, X. Ye, W. Guo, and A. Reykowski, A rapid and robust numerical algorithm for sensitivity encoding with sparsity constraints: self-feeding sparse SENSE, Magn Reson Med, 64, 1078–1088 **(2010)**.

[31] D. Liang, B. Liu, J. Wang, and L. Ying, Accelerating SENSE using compressed sensing, Magn Reson Med, 62, 1574-1584 **(2009)**.

[32] J. X. Ji, Z. Chen, and L. Tao, Compressed sensing parallel magnetic resonance imaging, Proceedings of the 30th Annual International Conference of the IEEE EMBS, **(2008)** August 20-25; British Columbia, Canada.

[33] M. Aharon, M. Elad, and A. Bruckstein, K-SVD: An algorithm for designing overcomplete dictionaries for sparse representation, IEEE Trans Signal Process*,* 54, 4311-4322 **(2006)**.

[34] J. F. Cai, H. Ji, Z. W. Shen, and G. B. Ye, Data-driven tight frame construction and image denoising, Appl Comput Harmon A*,* 37, 89-105 **(2014)**.

[35] Q. G. Liu, S. S. Wang, K. Yang, J. H. Luo, Y. M. Zhu, and D. Liang, Highly undersampled magnetic resonance image reconstruction using two-Level bregman method with dictionary updating, IEEE Trans Med Imaging*,* 32, 1290-1301 **(2013)**.

[36] X. B. Qu, Y. K. Hou, F. Lam, D. Guo, J. H. Zhong, and Z. Chen, Magnetic resonance image reconstruction from undersampled measurements using a patch-based nonlocal operator, Med Image Anal*,* 18, 843-856 **(2014)**.

[37] B. D. Ning, X. B. Qu, D. Guo, C. W. Hu, and Z. Chen, Magnetic resonance image reconstruction using trained geometric directions in 2D redundant wavelets domain and non-convex optimization, Magn Reson Imaging*,* 31, 1611-1622 **(2013)**.

[38] S. Fang and H. Guo, Nonlinear coil sensitivity estimation for parallel magnetic resonance imaging using data-adaptive steering kernel regression method , Proceedings of the 35th Annual International Conference of the IEEE EMBS, **(2013)** July 3-7; Osaka, Japan.

[39] L. Ying and J. Sheng, Joint image reconstruction and sensitivity estimation in SENSE (JSENSE), Magn Reson Med*,* 57, 1196-1202 **(2007)**.

[40] J. F. Yang, Y. Zhang, and W. Yin, A fast alternating direction method for TV L1-L2 signal reconstruction from partial Fourier data, IEEE J Sel Top Signal Process*,* 4, 288-297 **(2010)**.

[41] Y. Chen, X. Ye, and F. Huang, A novel method and fast algorithm for MR image reconstruction with significantly under-sampled data, Inverse Probl Imag*,* 4, 223-240 **(2010)**.

[42] X. Ye, Y. Chen, and F. Huang, Computational acceleration for MR image reconstruction in partially parallel imaging, IEEE Trans Med Imaging*,* 30, 1055-1063 **(2011)**.

[43] S. Mishra and R. Kappiyoor, Collimator Width Optimization in X-Ray Luminescent Computed Tomography (XLCT) with Selective Excitation Scheme, Journal of medical imaging and health informatics*,* 4, 641-686 **(2014)**.

[44] S. Ravishankar and Y. Bresler, MR image reconstruction from highly undersampled k-space data by dictionary learning, IEEE Trans Med Imaging, 30, 1028-1041, **(2011)**.

[45] Y. Wang, J. Yang, W. Yin, and Y. Zhang, A new alternating minimization algorithm for total variation image reconstruction, SIAM J Imaging Sci, 1, 248-272, **(2008)**.